Rose-derived 3D carbon nanosheets for high cyclability and extended voltage supercapacitors

Chongjun Zhao[*], Yaoxuan Huang, Chunhua Zhao, Xiaoxiao Shao, Zhaoqiang Zhu

Key Laboratory for Ultrafine Materials of Ministry of Education, Shanghai Key Laboratory of Advanced Polymeric Materials, School of Materials Science and Engineering, East China University of Science and Technology, Shanghai 200237, PR China

ARTICLE INFO

ABSTRACT

Biomass based porous carbon has been deemed to the most prospective electrode materials for high performance supercapacitors owing to its diversity and reproducibility. Herein, a three-dimensional (3D) porous structure consisting of interconnected carbon nanosheets were synthesized by withered rose through a convenient and efficient carbonization-activation method. This rose-derived active carbon nanosheets (RAC) display a high specific surface area ($1911 \, m^2 g^{-1}$) and a moderate bulk density ($0.55 \, g \, cm^{-3}$). RAC-based supercapacitor electrode exhibits a remarkable cycling stability of 99% capacitance retention after 25000 cycles even at a high specific capacitance of $208 \, F \, g^{-1}$. More importantly, its symmetric supercapacitor (SSC) owns an extended voltage window of 2.1 V and an excellent electrochemical stability (92% capacitance retention after 10000 cycles).

1. Introduction

Driven by global population growth, technology development, as well as social and economic progress, the requirement for resource and energy is increasing greatly, which eventually results in fossil fuels crisis and severe environmental contamination. In order to figure out this issue, it's urgent to not only exploit a green and renewable new energy sources but also develop clean and promising energy storage devices [1,2].

Supercapacitor, as a sort of electrochemical energy storage devices, has been attracted considerable attention over the last few decades due to its unique benefits such as higher energy density than electrostatic capacitors, shorter charge/discharge time, higher power density and better cyclability than batteries [3–5]. These features can balance the energy and power density conflict and thus make supercapacitors be a prospective candidate energy storage system for hybrid electric vehicle, mobile equipment and electrical engineering [6,7]. On the basis of the energy storage mechanism, supercapacitors can be divided into electric double-layer capacitors (EDLCs) depending on electrostatic charge diffusion and adsorption in a Helmholtz double layer formed at the electrode/electrolyte interface [8,9], and pseudocapacitors utilizing rapid and reversible faradaic reactions to store energy on the surface of active materials [10,11]. Although supercapacitor has many advantages, the low energy density still restrains its practical applications [12]. Therefore, it's an urgent requirement for supercapacitor to increase the energy density, keep the high power density and reduce the manufacturing cost.

For supercapacitor, according to the computational formula: $E = 1/2CV^2$, the energy density (E) is related to the capacitance (C) and voltage (V). The capacitance relies on the characteristics of electrode materials while the operating voltage is determined by the stable electrochemical window of active material and electrolyte. Therefore, the energy density of supercapacitor can be improved either by synthesizing high capacitance electrode materials or extending operating voltage window. The typical approach is using transition metal (Ru, Co, Fe, Mn, etc.) oxides composite materials to get higher capacitance [13], or nonaqueous electrolyte (acetonitrile or ionic liquid) which affords a wider operating voltage window [14]. However, both of the above two methods are highly toxic and expensive, which are inconsistent with the idea of environmentally friendly and low-cost. Based on these considerations, more and more efforts are being made on carbon materials in aqueous electrolyte due to their high specific surface area, relative high electrical conductivity, fast kinetic processes [15,16].

Recently, it is reported that the operating voltage window of carbon-based symmetric supercapacitor can reach to 1.8 V in the neutral electrolyte (Na_2SO_4) [17], higher than the theoretical decomposition potential value of water (1.23 V), but far from practical application. Therefore, it's promising to further widen the voltage so as to develop high energy density devices. Among the carbon materials, biomass-based activated carbon shows distinct competitiveness and superiority in supercapacitors market owing to controllable specific area, appropriate pore distribution, low production costs and reproducibility [18].

Up to now, multifarious biomass resources have been successfully used to prepare porous carbonaceous electrode materials with various morphologies and structures, including animal innards and pelage [19,20], insects [21], bacteria [22], fungi [23] and plants (embodying in their roots, stems, foliage, blooms, fructus and seeds) [24—27]. Obviously, the biomass-based activation carbon is still on the road from the fundamental research to the practical application. The challenges mainly consist of three parts: (1) improve comprehensive electrochemical performances include previously neglected or undeveloped ones, e.g., wide voltage window and long cyclability; (2) find new biomass candidates which can meet the practical requirement in large-scale, abundant and low-cost; (3) further modification of the current preparation methods. As the electrochemical performances are strongly depended on the intrinsic properties and preparation methods of activated carbon, the crucial points to overcome above three problems lie in finding the appropriate biomass candidates and optimizing the preparation conditions.

Among the above resources, plant-based biomass has been widely researched, because it principally contains cellulose, hemicellulose and xylogen, which are the suitable raw materials for activated carbon materials with abundant micropores, mesopores and macropores. Currently, the broad approaches to synthesize plant-derived porous carbon materials are chiefly direct pyrolysis, hydrothermal-assisted carbonization, and carbonization-activation under oxygen deficit conditions and below 1000 °C [28]. Among them, the carbonization-activation route is the most extensive approach, in which the precursors are carbonized under the flowing inert gases at first, and subsequently activated through physical (e.g., CO_2 [29] or steam [30]) and/or chemical (e.g., KOH [31], $ZnCl_2$ [32], or H_3PO_4 [33]) procedure at relatively high temperatures. Unlike carbonization-activation method, direct pyrolysis and hydrothermal-assisted carbonization usually result in low porosity (especially for micropore volume) and poor electrical conductivity [28,34], which will restrict the electrolyte penetration and limit the ability of charge transfer. However, the two-step carbonization-activation method can solve these problems. In this way, the resultant biomass carbon materials appear highly interconnected porous structures and large specific areas (up to 3000 $m^2 g^{-1}$), high extent of graphitization through the rise of temperature, and retain surface active functional groups via thermal treatment which removes the free and bound water as well as volatile carbon [31,35]. According to all the advantages mentioned above, we choose and optimize this convenient, efficient, mature and controllable carbonization-activation method to convert biomass into activated carbon. Hence, these glorious peculiarities ensure high activity and specific capacity, which make it possible to achieve large energy density and thus to be an alternative carbon material for supercapacitor applications.

Rose is a kind of perennial Rosa bush which can plant in many areas including North Korea, Japan, China and Europe due to its ornamental, medicinal and therapeutic values [36]. Because of its cheap and obtainable, it provides an abundant source to the synthesis of porous carbon materials. Besides, the rose petal possesses hierarchical porous structures consisting of microscale protrusions

with nanoscale wrinkles, which can offer plenty of reactive sites for ions/charges exchange [37]. Moreover, the rose also contains inorganic salts like potassium and magnesium salts which usually bring about numerous pores when react with hydrochloric acid [38]. In addition, the popularity of rose will attract much concern on biomass-based carbon, which may push the practical application of this method. As a result, rose can be a promising biomass carbon precursor for the establishment of porous carbon materials.

Herein, a simple and effective carbonization-activation two-step method is put forward to transform low-cost withered rose into three-dimensional (3D) interconnected carbon nanosheets for high performance supercapacitors. The rose is preliminary carbonized at 600 °C to obtain the fundamental carbon frameworks and further activated with KOH at higher temperatures. During the activation process, KOH serves as a template to restrain adjacent roses from fusing/agglomerating, and an activating agent which reacts with inner carbon to produce gases and create abundant porous structures. Consequently, the resultant rose-based activated carbon nanosheets have high surface area (1911 $m^2 g^{-1}$), moderate bulk density (0.55 $g cm^{-3}$) and 3D hierarchically interconnected porous structures. As a result, the as-obtained activated carbon electrode displays a relatively high gravimetric capacitance of 208 $F g^{-1}$ at 0.5 $A g^{-1}$ and remarkable cycling stability (99% capacitance retention after 25000 cycles at a high current density of 10 $A g^{-1}$). Moreover, a symmetric supercapacitor based on the as-fabricated RAC delivers an extended voltage window of 2.1 V and a high energy density of 20.32 $Wh kg^{-1}$ at 525 $W kg^{-1}$ together with excellent cyclability (about 92% capacitance retention after 10000 cycles at 5 $A g^{-1}$).

2. Experimental

2.1. Synthesis of electrode materials

Typically, the withered roses were washed with ethyl alcohol and deionized water under ultrasonic condition, and dried at 60 °C in an oven overnight. Afterwards, the pretreated roses were added into a corundum crucible and heated in a tubular furnace at 600 °C for 2 h under N_2 atmosphere. The rose-derived pre-carbonized products were obtained and termed as RPC.

RPC was ground uniformly with a certain proportion of potassium hydroxide in solid phase. Subsequently, the homogenous mixture was collected and then transferred to a tubular furnace to suffer a temperature at 750—900 °C for 1.5 h in flowing N_2. Finally, the obtained activated carbon was thoroughly rinsed with 1.0 M HCl solution and deionized water and further dried in an oven at 60 °C for 24 h. The final active carbon samples were denoted as RAC-T-x, where T (T = 750, 800, 850 or 900) stands for the activation temperatures, and x indicates the mass proportion of KOH (RPC was maintained a constant at 1). For instance, RAC-800-2 represents the sample was synthesized at 800 °C with a mass proportion of KOH/RPC = 2. For comparison, RPC was calcined at 800 °C without adding KOH and the obtained sample was labeled as RAC-800-0.

2.2. Materials characterization

The phase analysis of fabricated samples were conducted by X-ray diffractometer (XRD, RIGAKU, D/MAX 2550 V) with Cu Kα radiation ($\lambda = 0.15406$ nm). Raman spectra were recorded by using a Raman microprobe (INVIA, Renishaw Instruments, England) with 514 nm laser excitation. The morphology and microstructure of the samples were confirmed by field emission scanning electron microscopy (FESEM, Hitachi, S-4800) and transmission electron microscopy (TEM, JEOL, JEM-2100). Thermogravimetric analysis (TGA)

was measured on a NETZSCH STA 409 analyzer from 20 to 1000 °C at a heating rate of 10 °C min^{-1} under N$_2$ atmosphere. The specific area, pore size distribution, total pore volume (V_T) and other porous texture were revealed by nitrogen adsorption-desorption analysis at 77 K (Micromeritics ASAP 2010).

2.3. Electrochemical measurements

The electrochemical performances of rose-derived electrodes were measured on a CHI 660E electrochemical workstation by using a standard three-electrode system in 6.0 M KOH aqueous solution. The working electrode was fabricated by thoroughly mixing the as-prepared active materials, acetylene black and poly-vinylidene fluoride (PVDF) with a mass ratio of 8:1:1 in N-methyl-2-pyrrolidone (NMP) to form a slurry. Then the slurry was coated onto a nickel foam (NF) current collector with an area of 1×1 cm^2. After dried at 60 °C overnight, the nickel foam was pressed under a pressure of 10 MPa to obtain the final working electrode. The mass loading of active material in each electrode was ca. 3 mg cm^{-2}. A platinum foil (2×3 cm^2) and a saturated calomel electrode (SCE) were served as the counter and reference electrodes, respectively. The cycle voltammetry (CV) and galvanostatic charge/discharge (GCD) curves were investigated within a potential windows of -1.2 V to 0 V. The electrochemical impedance spectroscopy (EIS) was measured with an AC voltage amplitude of 5 mV in the frequency range from 0.01 Hz to 100 kHz at open circuit potential. The symmetric supercapacitor (SSC) was assembled by using two rose-based electrodes with just the same mass loading and size, and the electrochemical performances of symmetric supercapacitor was measured in an operating voltage range of $0-2.1$ V in 1.0 M Na$_2$SO$_4$ aqueous solution.

The specific capacitance of electrodes can be calculated from the charge/discharge curves according to the following equation:

$$C_g = \frac{I \times \Delta t}{m \times \Delta V} \tag{1}$$

where C_g (F g^{-1}) is the specific capacitance based on the mass of the active materials, I (A) is the discharge current, Δt (s) is the discharge time, m (g) is the mass loading of the active materials of electrode, ΔV (V) is the discharge potential range.

The energy density E (Wh kg^{-1}) and power density P (W kg^{-1}) can be calculated by using the following equations:

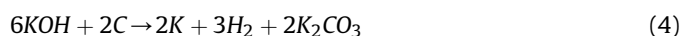$$E = \frac{1}{2}C_g \times \Delta V^2 \times \frac{1}{3.6} \tag{2}$$

$$P = \frac{E}{\Delta t} \times 3600 \tag{3}$$

where C_g (F g^{-1}) is specific capacitance of the supercapacitor measured from Eq. (1), ΔV (V) is the applied voltage range within the discharge time Δt (s).

3. Results and discussion

The RAC was obtained from the carbonization-activation procedure given in Scheme 1. Referring to the temperature for RAC sample, it was determined based on thermogravimetric analysis (TGA). As shown in Fig. S1, when the temperature increases to 600 °C, the rate of weight loss become balance, indicating the accomplishment of carbonaceous transformation. Therefore, at the pre-carbonization temperature of 600 °C, thermal decomposition and polycondensation reactions of organic compounds occur, which results in the breakage of cell walls and formation of fundamental carbon skeleton (Fig. S2a and b) [39]. Then, during the activation process, KOH fuses and breaks the surface chemical bond, and thus promotes ions intercalate into the rose lamellas, which makes roses present a 3D interconnected carbon nanosheets (Fig. S2c and d). For comparison, as shown in Fig. S2e and f, the carbon skeleton in RPC turns into lamellas with ravine in the absence of KOH. Therefore, the activated chemical reactions can be suggested as the following equations:

$$6KOH + 2C \rightarrow 2K + 3H_2 + 2K_2CO_3 \tag{4}$$

$$K_2CO_3 \rightarrow K_2O + CO_2 \tag{5}$$

$$CO_2 + C \rightarrow 2CO \tag{6}$$

$$K_2CO_3 + 2C \rightarrow 2K + 3CO \tag{7}$$

$$C + K_2O \rightarrow 2K + CO \tag{8}$$

KOH or K$_2$CO$_3$ can not only overcome the van der Waals force between the graphitic layers, but also create homogeneous erosion, which generates microporous, mesoporous and macroporous structure [40]. Moreover, the carbon yield is about 24% for the RAC-800-0 as confirmed by TGA (Fig. S1). The carbon yield reduces with the increase of activation temperature (Table S1), confirming the accelerative impact of rising temperature.

The morphologies of as-obtained RAC under different activation temperatures are shown in SEM images in Fig. 1. Owing to the relatively low temperature, the thick carbon sheets in RAC-750-2 sample (Fig. 1a) are not fully etched and there are also some carbon particles due to the incomplete stripping of RPC. It is reasonable assumed that the fragile margins of roses were initially shattered into debris and hard veins held supporting frameworks. As the activation temperature reached 800 °C, the as-prepared carbon nanosheets become much rougher and thinner with a thickness of around 100 nm (Fig. 1b). At the moment, the erosion of KOH is moderate and uniform, which leads to the formation of wrinkled 3D interconnected porous networks consisting of carbon nanosheets. On increasing the activation temperature up to 850 °C, as shown in Fig. 1c, obviously, the corbelled frameworks begin to collapse and the 3D interconnected nanosheets turn into two-dimensional (2D) nanosheets. Furthermore, when the temperature extends to 900 °C, the framework is almost completely cracked and nanosheets became slippy (Fig. 1d). With a view to different activation temperatures (750, 800, 850 and 900 °C), SEM image of RAC-800-2 shows 3D interconnected porous networks, which can bring a large specific area and sufficient active sites for electrochemical reaction.

Simultaneously, high-resolution transmission electron microscopy (HRTEM) images of RAC-800-2 (Fig. 2) further demonstrate the porous construction including micropores and mesopores, indicating the intense activation of KOH. An SAED pattern also confirms the amorphous nature of the obtained carbon (the inset of Fig. 2d), which is consistent with the following XRD pattern as shown in Fig. 3a. Such porous structure can enlarge the specific surface area, shorten ion transmission path and promote charge accumulation, and eventually result in high energy storage. To investigate the effect of the mass ratio of KOH on morphological evolution, SEM images of the samples are compared. As shown in Fig. S3, with the increasing of KOH addition, the reaction (eq. (4)) between carbon and KOH will be pushed, which leads to form pores and raise frameworks (Fig. S3b), further causes the generation of interconnected porous nanosheets networks (Fig. S3c). However, the nanosheets are broken and aggregated into irregular block in RAC-800-3 (Fig. S3d) due to the excessive etch.
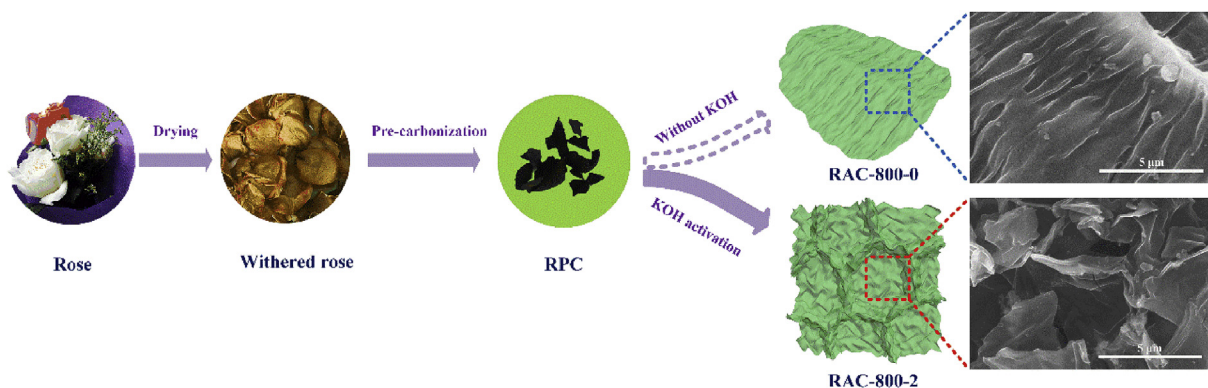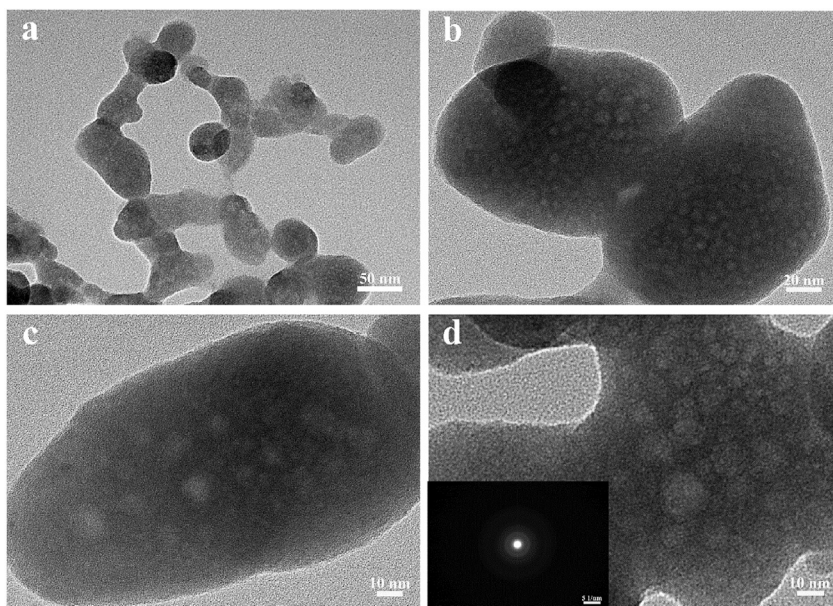
Scheme 1. Schematic illustration of the formation of rose-based carbon nanosheets.
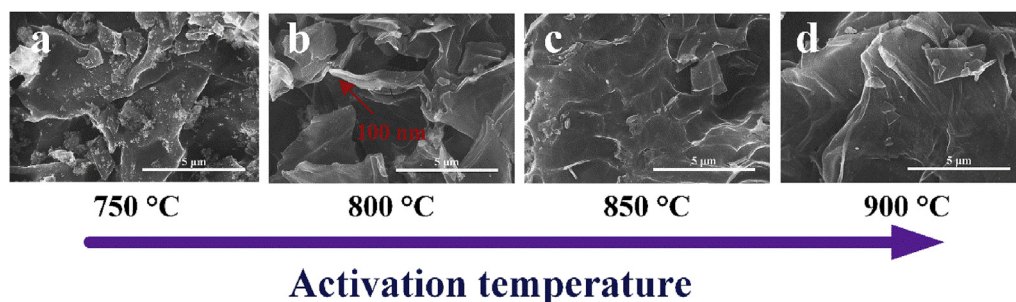
Fig. 1. The SEM images of RAC-750-2 (a), RAC-800-2 (b), RAC-850-2 (c) and RAC-900-2 (d).


Fig. 2. The TEM images of RAC-800-2 at different magnifications (a–d). The inset of d is the SAED pattern.

X-ray diffraction analysis (XRD, Fig. 3a) presents two broad diffraction peaks at 2θ of ~24° and ~43°, indexing to (002) and (100) planes of graphite, which are consistent with the dominate features of amorphous carbon. For RAC-800-2, the (002) peak shifts to a lower angle in comparison to RPC and RAC-800-0, signifying larger interlayer spacing as a result of the porous frameworks, which is consistent with SEM observations (Fig. 1b). The Raman spectroscopy analysis was carried out to further evaluate the graphitic

textural characteristics (Fig. 3b). The relative intensity ratio of D band and G band (I_D/I_G) is used to indicate the degree of graphitization and defects [10]. As shown in Table 1, with the increase of activation temperature, the I_D/I_G values gradually increase (from 0.83 to 0.92), testifying the appearance of more defect sites, which is in accordance with XRD analysis.

The porous texture of the obtained carbon samples is evaluated by N_2 adsorption/desorption isotherm analysis and the results are
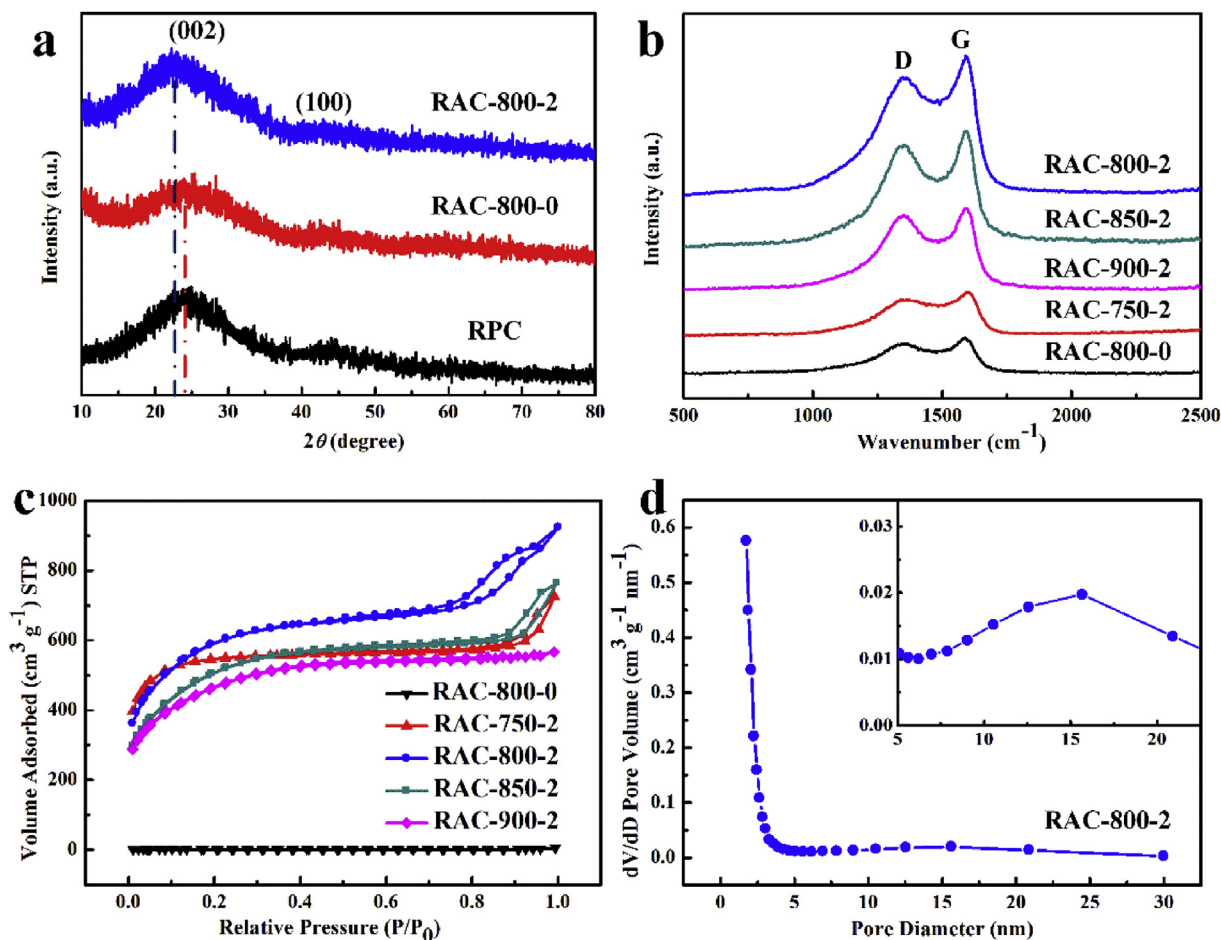
Fig. 3. The XRD patterns of RPC, RAC-800-0 and RAC-800-2 (a). The Raman spectrum of RAC samples (b). N_2 adsorption/desorption isotherms of RAC samples (c). The pore size distribution curve of RAC-800-2 (d), the inset is the enlarged image.

Table 1
Physical and electrochemical properties of the as-prepared carbon materials.

Sample	S_{BET} [a] [m^2 g^{-1}]	V_{total} [b] [cm^3 g^{-1}]	V_{micro} [c] [cm^3 g^{-1}]	APS [d] [nm]	I_D/I_G	C_g [e] [F g^{-1}]
RAC-800-0	2.908	0.0027	0.0005	3.76	0.84	72.9
RAC-750-2	1646	0.958	0.648	2.33	0.83	191.7
RAC-800-2	1911	1.319	0.264	2.76	0.85	208.0
RAC-850-2	1687	1.025	0.114	3.01	0.88	190.3
RAC-900-2	1548	0.856	0.182	2.21	0.92	182.1

[a] Specific surface area based on Brunauer-Emmett-Teller (BET) equation.
[b] The total pore volume was concluded from nitrogen adsorption at a relative pressure of 0.95.
[c] The micropore volume obtained from t-plot method.
[d] Adsorption average pore size.
[e] Gravimetric capacitance obtained at a current density of 0.5 A g^{-1} in 6.0 mol L^{-1} KOH based on three-electrode system.

described in Fig. 3c. Unlike RAC-800-0 which shows a type I adsorption/desorption isotherm, RAC-750-2, RAC-800-2, RAC-850-2 and RAC-900-2 exhibit the typical type IV isotherms with high platform at middle pressure and an apparent type H4 hysteresis loop at $P/P_0 > 0.45$, demonstrating the co-existence of micropores and mesopores [41,42]. Comparing with RAC-800-0, RAC-800-2 exhibits a noticeable increased N_2 adsorption in the relative pressure range of 0.8—1.0, suggesting the intense activation and template function of KOH. With the increase of activation temperature, the isotherms become gentler at low pressure, which proves the microporous structure evolution influenced by temperature. The pore size distribution curve (PSD) of the RAC-800-2 sample was estimated by the Barrett-Joyner-Halenda (BJH) model to the adsorption branch of the isotherm. As shown in Fig. 3d, RAC-800-2 sample presents micropores mainly located at 1.77 nm and continuous mesopores distribution in the range of 5—20 nm (the inset of Fig. 3d), which is in good agreement with the observation of TEM. The detailed textural properties of as-prepared RAC samples are calculated by the Brunauer-Emmett-Teller (BET) model and the results are generalized in Table 1. Clearly, the specific surface area (SSA) and pore volume increase with activation temperature from 750 °C to 800 °C, however, they decrease when the temperature further rises. These results manifest the generation of pores under 800 °C as well as the agglomeration and collapse process at higher temperature. Therefore, RAC-800-2 sample delivers a high SSA of 1911 m^2 g^{-1} and a pore volume of 1.319 cm^3 g^{-1}. Such

interconnected porous frameworks and high SSA of RAC-800-2 can afford adequate active sites for charges/ions accumulation and exchange, which is a favor to excellent electrochemical performances.

The electrochemical performances of the RAC-based electrodes were assessed in 6.0 M KOH aqueous electrolyte in three-electrode system by feat of cyclic voltammetry (CV), galvanostatic charge/

discharge (GCD) and electrochemical impedance spectroscopy (EIS). Fig. 4a compares the CV curves of RAC-800-0, RAC-750-2, RAC-800-2, RAC-850-2 and RAC-900-2 at a scan rate of 100 mV s^{-1}. Obviously, the CV curve of RAC-800-0 has the severe distortion from rectangle and smallest loop area, testifying the tiny specific capacitance, which is accord with its low SSA and total pore volume. As the activation temperature increases, the shape of CV
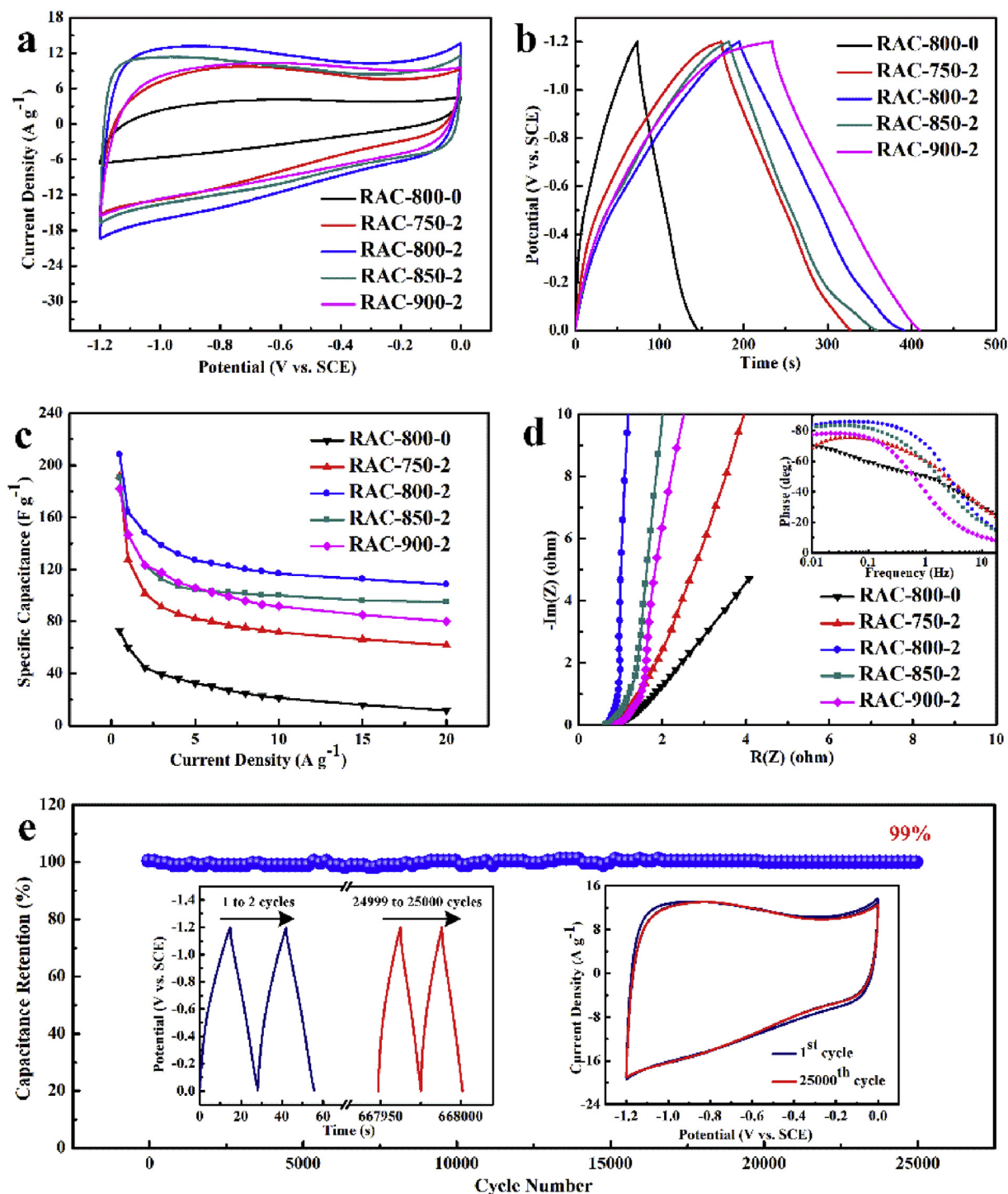
Fig. 4. Electrochemical performance of the as-prepared carbon samples in 6.0 M KOH aqueous electrolyte in a three-electrode system. Comparison of the CV curves at 100 mV s^{-1} (a). The GCD profiles at 1 A g^{-1} (b). The specific capacitance *versus* different current densities (c). The Nyquist plots (d), the inset shows the phase angle *versus* frequency. Cycling stability of RAC-800-2 after 25000 cycles at 10 A g^{-1} (e), the inset shows the GCD curves of the initial two cycles and the last two cycles of 25000 cycles (left), and the CV curves before cycling and after 25000 cycles (right).

curves become more and more rectangular and the RAC-800-2 sample exhibits the largest current response, revealing excellent EDLC behaviors. The CV curves of as-prepared RAC samples acquired at scan rates from 20 to 300 mV s^{-1} are shown in Fig. S4 and S5. For RAC-800-2, CV curves still maintains a quasi-rectangular shape even at a scan rate of 300 mV s^{-1}, displaying outstanding rate performance and stability, which is attributed to the 3D interconnected porous nanosheets frameworks that enhance the pore accessibility and shorten ion diffusion distance. The GCD curves of RAC-800-0, RAC-750-2, RAC-800-2, RAC-850-2 and RAC-900-2 samples at a current density of 1 A g^{-1} are illustrated in Fig. 4b. As seen, RAC-800-2 delivers the longest discharge time and its GCD curve appears an almost linear and symmetric shape, which also proves the preferable electrochemical reversibility. Furthermore, the IR drop of RAC-800-2 (0.003 V) is just one sixth as that of RAC-800-0 (0.018 V), signifying a minuscule internal resistance. The GCD curves of RAC samples at various current densities from 0.5 to 20 A g^{-1} are shown in Fig. S4 and S5. The specific capacitances *versus* different current densities are calculated and given in Fig. 4c. In accordance with CV results, RAC-800-2 sample presents the maximal specific capacitance (208 F g^{-1} at 0.5 A g^{-1}) contrasted to other RAC samples. Even at a high charge-discharge rate of 20 A g^{-1}, the RAC-800-2 still remains a specific capacitance of 108.3 F g^{-1}, which is almost as ten-fold as that of RAC-800-0 (*e.g.* 11 F g^{-1}), revealing excellent rate capability. For a better comparison, the specific capacitances of RAC-800-2 as well as previously published carbon-based electrodes are listed in Table 2 [43—51].

EIS curves also reflect the electrochemical performance of the obtained samples and the results are displayed in Fig. 4d. The Nyquist plot is composed of a steep straight line in low frequency region representing an ideal capacitive behavior and the ion diffusion resistance, as well as a semicircle in the high frequency region indicating the charge transfer resistance (R_{ct}). Meanwhile, the intersection of the semicircle and the X-axis reflects the internal resistance. Obviously, the RAC-800-2 sample exhibits the steepest slope, meaning the fast diffusion of ions. In the Bode phase diagrams (the inset of Fig. 4d), the phase angle of RAC-800-2 is about 84°, which is close to the ideal capacitor behavior (90°) [52]. For comparison, the phase angle of RAC-800-0, RAC-750-2, RAC-850-2 and RAC-900-2 are only 70°, 69°, 82° and 77°, respectively. Moreover, the operating frequency (f_0) when the capacitance has half of maximum is 3.16 Hz for RAC-800-2, offering the relaxation time constant ($\tau_0 = 1/f_0$, the minimum time that a device required to remove all the energy) of 0.32 s, which are the momentous quantitative indexes of the speed for reversible charging-discharging of electrodes [52].

The cycling stability is also a referential property to demonstrate the durability of RAC-based electrodes. As shown in Fig. 4e, the capacitance retention of RAC-800-2 sample exhibits a slight decrease (about 1%) of the initial specific capacitance after 25000 cycles. This glorious electrochemical cyclability is probably correlated with the interconnected porous nanosheets structures and

wettability. The interconnected porous nanosheets can reserve electrolytes and shorten transport path, more importantly, they can keep a stable foundation architecture even at a large current charge/discharge process. The wettability of materials is enhanced with the increasing of soaking time, which is beneficial to the accessibility of electrolytes to pores and the fast diffusion of ions. Notably, the CV curves after 25000 cycles (the inset of Fig. 4e, right) are basically the same as that before cycling, indicating a superior cyclability.

The electrochemical performances and practical behaviors of the RAC-800-2 electrode were further evaluated based on a two-electrode symmetric supercapacitor (SSC). In order to compare the influence of different electrolytes and explore the most suitable one, a RAC-800-2//RAC-800-2 symmetric supercapacitor was fabricated and measured in 6.0 M KOH and 1.0 M Na$_2$SO$_4$ aqueous electrolyte separately. As shown in Fig. S6a and b, the RAC-800-2// RAC-800-2 supercapacitor displays a good capacitive behavior within the voltage window of 0—1.5 V in 6.0 M KOH. However, the maximum specific capacitance and voltage window in 6.0 M KOH are lower than that in 1.0 M Na$_2$SO$_4$ (Fig. S6c and d). In view of the wider operating voltage window, less corrosion and better safety, 1.0 M Na$_2$SO$_4$ aqueous electrolyte was eventually chosen.

To further confirm the stable operating voltage window of the device in 1.0 M Na$_2$SO$_4$ aqueous electrolyte, RAC-800-2//RAC-800-2 symmetric supercapacitor was tested in different voltage ranges from 2.0 V to 2.4 V at 100 mV s^{-1} (Fig. 5a). It is noted that CV curve still retains a perfect rectangular shape even at 2.1 V without obvious increase of anodic current, indicating an ideal capacitive behavior and excellent reversibility. As previously reported, the operating voltage window can be extended in neutral aqueous electrolyte, which is attributed to the high overpotential for di-hydrogen evolution caused by the low H$^+$ and OH$^-$ concentration or the strong solution of cations and anions [53,54]. Furthermore, the 3D interconnected porous structure can also enlarge the voltage window. The porous structures provide plenty of active sites for H$^+$ adsorption and large interlayer spacing facilitate the H$^+$ insertion, which may inhibit di-hydrogen evolution in electrolyte [55]. In addition, the extended voltage window maybe also attributed to the existence of oxygen-containing functional groups introduced by KOH activation process. The content of oxygen-containing functional group of KOH activated carbon is higher than that of carbon materials without activation, which can make more contribute to operating voltage window [15]. The wide voltage window of 2.1 V is higher than those of previous carbon-based aqueous SSC [39,40,43,52,54,56—66] (as listed in Table 3) and can not only markedly enlarge the energy density but also reduce the number of series equipment for the expected output voltage. CV curves of RAC-800-2//RAC-800-2 symmetric supercapacitor within the voltage window of 0—2.1 V remain rectangular-like shape even at a high scan rate of 300 mV s^{-1} (Fig. 5b), indicating a decent capacitive behavior and excellent rate capability.

Table 2
Comparison of electrochemical performances of carbon-based electrodes.

Carbon type	Activating agent	Specific capacitance (F g^{-1})	Measurements done at	Electrolyte type	Cycling stability	Ref.
Shrimp shells derived carbon	H$_3$PO$_4$	175	0.5 A g^{-1}	6.0 M KOH	94%, 1000 cycles	[43]
Cigarette filter derived carbon	NH$_3$	153.8	1 A g^{-1}	6.0 M KOH	Slight increase, 6000 cycles	[44]
Rice husk derived carbon	H$_3$PO$_4$	112	1 A g^{-1}	1.0 M Na$_2$SO$_4$	None	[45]
Microalgae derived carbon	KOH	200	0.1 A g^{-1}	1.0 M LiCl	98%, 10000 cycles	[46]
Banana fibers derived carbon	ZnCl$_2$	74	0.5 A g^{-1}	1.0 M Na$_2$SO$_4$	88%, 500 cycles	[47]
Hexaporous carbon	None	154	0.5 A g^{-1}	1.0 M H$_2$SO$_4$	Slight decrease, 1000 cycles	[48]
Pillared graphene paper	None	138	10 mV s^{-1}	6.0 M KOH	96.15%, 2000 cycles	[49]
MWCN/activated CNFs	Steam	160	0.5 A g^{-1}	6.0 M KOH	94%, 1000 cycles	[50]
Cherry blossom petals derived carbon	Air	20	10 A g^{-1}	0.5 M KCl	92.3%, 10000 cycles	[51]
Rose-derived carbon	KOH	208	0.5 A g^{-1}	6.0 M KOH	99%, 25000 cycles	This work
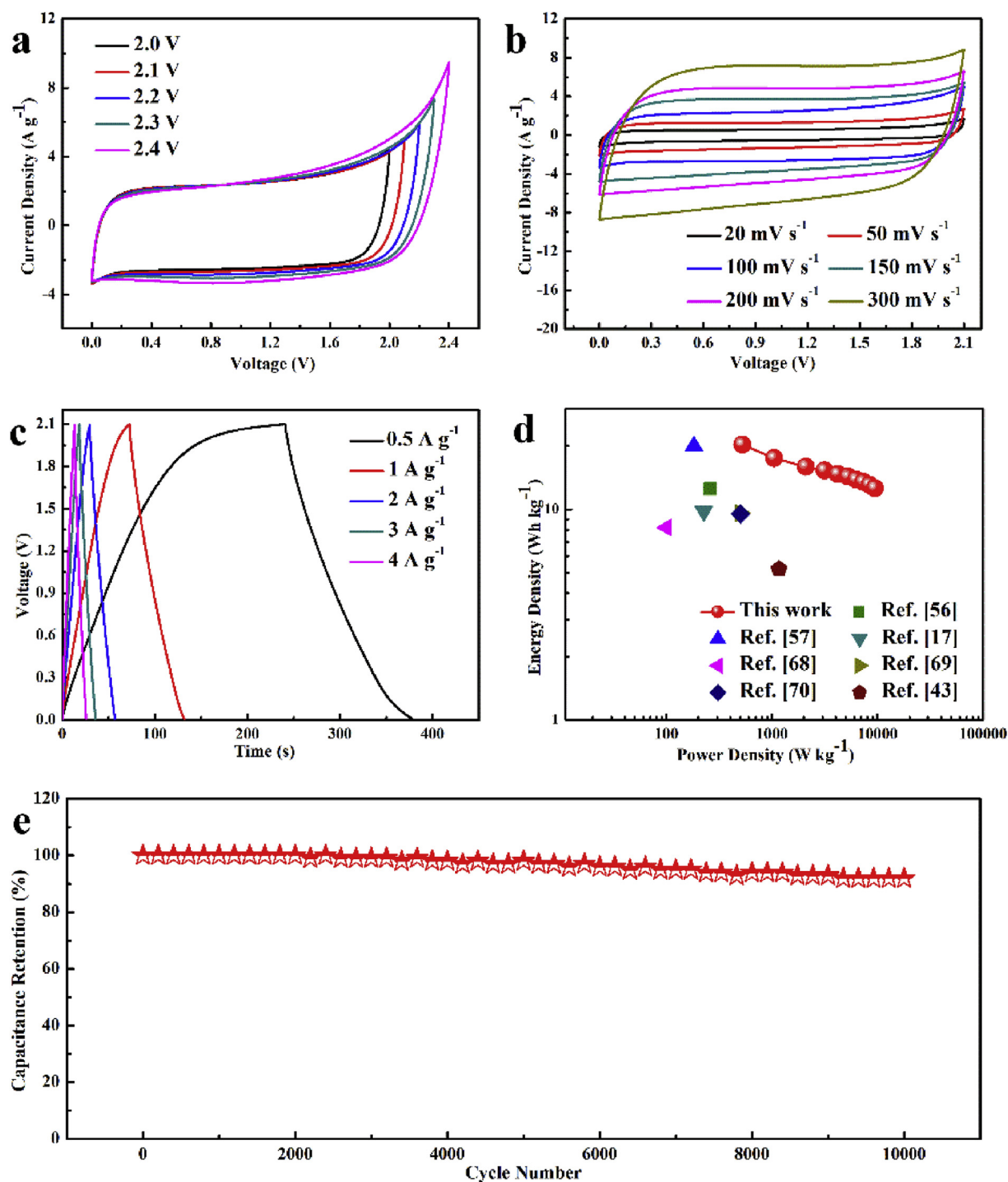
Fig. 5. Electrochemical characteristics of the RAC-800-2//RAC-800-2 symmetric supercapacitor in 1.0 M Na$_2$SO$_4$ aqueous electrolyte in a two electrode system. The CV curves in different voltage windows at 100 mV s^{-1} (a). The CV curves in 2.1 V at different scan rates (b). The GCD profiles at different current densities (c). The Ragone plots of our symmetric supercapacitor and other previously reported carbon-based symmetric supercapacitor in aqueous electrolytes (d). Cycling stability of the RAC-800-2//RAC-800-2 symmetric supercapacitor after 10000 cycles at 5 A g^{-1} (e).

As shown in Fig. 5c, GCD curves of RAC-800-2//RAC-800-2 symmetric supercapacitor delivers approximate liner shape with low IR drop (0.03 V at 1 A g^{-1}), manifesting reversible charge-discharge performance and small internal series resistance. The calculated specific capacitance based on GCD curves was calculated to be 33.2, 28.6, 26.0, 25.0 and 24.0 F g^{-1} at current densities of 0.5, 1, 2, 3 and 4 A g^{-1}, respectively. Note that the capacitance value of the two-electrode system is strongly decided by the configuration

of cells and the total mass of active materials in positive/negative electrodes. Moreover, it is also closely related to the size of solvated cation/anion and the equilibrium potential of both electrodes [67].

The energy and power densities of RAC-800-2//RAC-800-2 symmetric supercapacitor are summarized in Fig. 5d. It is clearly observed that RAC-800-2//RAC-800-2 supercapacitor exhibits a high energy density of 20.32 Wh kg^{-1} at a power density of 525 W kg^{-1}, higher than those of carbon-based symmetric

Table 3
Comparison of electrochemical test conditions of different carbon-based supercapacitors.

Carbon type	Three-electrode system		Two-electrode system			Ref.
	Electrolyte type	Potential range (V)	Assembled type	Electrolyte type	Voltage window (V)	
Perilla frutescens derived carbon	6.0 M KOH	0 ~ −1.0	SSC	1.0 M Na$_2$SO$_4$	1.8	[39]
Fungus derived carbon	6.0 M KOH	0 ~ −1.0	SSC	1.0 M Na$_2$SO$_4$	1.8	[40]
Shrimp shells derived carbon	6.0 M KOH	−0.1 ~ −0.9	SSC	6.0 M KOH	1.1	[43]
Tofu derived carbon	6.0 M KOH	0 ~ −1.0	SSC	1.0 M Na$_2$SO$_4$	1.8	[52]
Lotus seedpods derived carbon	6.0 M KOH	0 ~ −1.0	SSC	6.0 M KOH	1.0	[56]
Bagasse wastes derived carbon	6.0 M KOH	0 ~ −1.0	SSC	1.0 M Na$_2$SO$_4$	1.8	[57]
Wool fiber derived carbon	6.0 M KOH	0 ~ −1.0	SSC	0.5 M Na$_2$SO$_4$	1.8	[58]
Tea-leaves based carbon	2.0 M KOH	0 ~ −1.0	SSC	0.5 M Na$_2$SO$_4$	1.8	[59]
Pomelo mesocarps derived carbon	2.0 M KOH	0 ~ −1.0	SSC	0.5 M Na$_2$SO$_4$	1.8	[60]
Soya derived carbon	1.0 M H$_2$SO$_4$	0.9 ~ −0.3	SSC	1.0 M H$_2$SO$_4$	1.5	[61]
ZIF-8 derived porous carbon	6.0 M KOH	0 ~ −1.0	SSC	1.0 M Na$_2$SO$_4$	1.8	[62]
Polysiloxane derived porous carbon	6.0 M KOH	0 ~ −1.0	SSC	1.0 M LiNO$_3$	1.8	[63]
Silkworm excrement derived carbon nanosheets	6.0 M KOH	0 ~ −1.0	SSC	1.0 M Na$_2$SO$_4$	2.0	[64]
CNTs/CC	0.5 M Na$_2$SO$_4$	1.0 ~ −1.0	SSC	0.5 M Na$_2$SO$_4$	2.0	[65]
MnOOH/CC	0.5 M LiNO$_3$	0.8 ~ −0.9	SSC	0.5 M LiNO$_3$	1.7	[66]
MnO$_2$@CNTs/Ni	1.0 M Na$_2$SO$_4$	0.8 ~ −0.2	SSC	1.0 M Na$_2$SO$_4$	2.0	[54]
Rose derived carbon	6.0 M KOH	0 ~ −1.2	SSC	1.0 M Na$_2$SO$_4$	2.1	This work

supercapacitors from different biomass sources including shrimp shells (5.2 Wh kg^{-1} at 1162 W kg^{-1}) [43], lotus seedpods (12.5 Wh kg^{-1} at 260 W kg^{-1}) [56], bagasse wastes (20 Wh kg^{-1} at 182 W kg^{-1}) [57], sorghum stalk (9.77 Wh kg^{-1} at 225.35 W kg^{-1}) [17], shiitake mushroom (8.2 Wh kg^{-1} at 100 W kg^{-1}) [68], coconut shell (9.58 Wh kg^{-1} at 500 W kg^{-1}) [69], catkins (9.5 Wh kg^{-1} at 500 W kg^{-1}) [70]. The cyclability of RAC-800-2//RAC-800-2 symmetric supercapacitor displays 92% capacitance retention after 10000 cycles at 5 A g^{-1} (Fig. 5e), demonstrating excellent electrochemical cyclability.

4. Conclusions

In summary, rose-derived interconnected carbon nanosheets with 3D porous structure was successfully produced by a convenient and efficient carbonization-activation method. Owing to the hierarchical porous frameworks, high specific surface area, moderate bulk density and centralized pore size distribution, the optimized RAC-800-2-based electrode displays a high specific capacitance of 208 F g^{-1} at 0.5 A g^{-1}, and a remarkable cyclability of 99% capacitance retention after 25000 cycles at 10 A g^{-1}. More importantly, the assembled RAC-800-2//RAC-800-2 symmetric supercapacitor delivers an extended voltage window of 2.1 V and a superb energy density of 20.32 Wh kg^{-1} at 525 W kg^{-1} with an excellent electrochemical stability of 92% capacitance retention after 10000 cycles. Therefore, a potential strategy that employing cheap and eco-friendly biomass to prepare electrode materials for high performance supercapacitors was supplied.

Acknowledgements

Appendix A. Supplementary data

Supplementary data to this article can be found online at https://doi.org/10.1016/j.electacta.2018.09.136.

References

[1] F.-X. Ma, L. Yu, C.-Y. Xu, X.W. Lou, Self-supported formation of hierarchical NiCo2O4 tetragonal microtubes with enhanced electrochemical properties, Energy Environ. Sci. 9 (2016) 862–866.

[2] L. Zhang, S.X. Dou, H.K. Liu, Y. Huang, X. Hu, Symmetric electrodes for electrochemical energy-storage devices, Adv. Sci. 3 (2016), 1600115.

[3] G. Wang, L. Zhang, J. Zhang, A review of electrode materials for electrochemical supercapacitors, Chem. Soc. Rev. 41 (2012) 797–828.

[4] J. Yan, Q. Wang, T. Wei, Z. Fan, Recent advances in design and fabrication of electrochemical supercapacitors with high energy densities, Adv. Energy Mater. 4 (2014).

[5] Z. Chen, Y. Yuan, H. Zhou, X. Wang, Z. Gan, F. Wang, Y. Lu, 3D nanocomposite architectures from carbon-nanotube-threaded nanocrystals for high-performance electrochemical energy storage, Adv. Mater. 26 (2014) 339–345.

[6] C. Long, T. Wei, J. Yan, L. Jiang, Z. Fan, Supercapacitors based on graphene-supported iron nanosheets as negative electrode materials, ACS Nano 7 (2013) 11325–11332.

[7] G. Zhang, X.W. Lou, General solution growth of mesoporous NiCo2O4 nanosheets on various conductive substrates as high-performance electrodes for supercapacitors, Adv. Mater. 25 (2013) 976–979.

[8] H. Jiang, P.S. Lee, C. Li, 3D carbon based nanostructures for advanced supercapacitors, Energy Environ. Sci. 6 (2013) 41–53.

[9] H. Ji, X. Zhao, Z. Qiao, J. Jung, Y. Zhu, Y. Lu, L.L. Zhang, A.H. MacDonald, R.S. Ruoff, Capacitance of carbon-based electrical double-layer capacitors, Nat. Commun. 5 (2014) 3317.

[10] Z. Li, Z. Xu, H. Wang, J. Ding, B. Zahiri, C.M.B. Holt, X. Tan, D. Mitlin, Colossal pseudocapacitance in a high functionality–high surface area carbon anode doubles the energy of an asymmetric supercapacitor, Energy Environ. Sci. 7 (2014) 1708–1718.

[11] V. Augustyn, P. Simon, B. Dunn, Pseudocapacitive oxide materials for high-rate electrochemical energy storage, Energy Environ. Sci. 7 (2014) 1597–1614.

[12] P. Simon, Y. Gogotsi, Materials for electrochemical capacitors, Nat. Mater. 7 (2008) 845–854.

[13] W. Li, K. Xu, B. Li, J. Sun, F. Jiang, Z. Yu, R. Zou, Z. Chen, J. Hu, MnO2 nanoflower arrays with high rate capability for flexible supercapacitors, Chem. Electr. Chem. 1 (2014) 1003–1008.

[14] J. Jiang, High temperature monolithic biochar supercapacitor using ionic liquid electrolyte, J. Electrochem. Soc. 164 (2017) H5043–H5048.

[15] Y. Cheng, B. Li, Y. Huang, Y. Wang, J. Chen, D. Wei, Y. Feng, D. Jia, Y. Zhou, Molten salt synthesis of nitrogen and oxygen enriched hierarchically porous carbons derived from biomass via rapid microwave carbonization for high voltage supercapacitors, Appl. Surf. Sci. 439 (2018) 712–723.

[16] B. Duan, X. Gao, X. Yao, Y. Fang, L. Huang, J. Zhou, L. Zhang, Unique elastic N-doped carbon nanofibrous microspheres with hierarchical porosity derived from renewable chitin for high rate supercapacitors, Nano Energy 27 (2016) 482–491.

[17] G. Ma, F. Hua, K. Sun, Z. Zhang, E. Feng, H. Peng, Z. Lei, Porous carbon derived from sorghum stalk for symmetric supercapacitors, RSC Adv. 6 (2016) 103508–103516.

[18] A.M. Abioye, F.N. Ani, Recent development in the production of activated carbon electrodes from agricultural waste biomass for supercapacitors: a review, Renew. Sustain. Energy Rev. 52 (2015) 1282–1293.

[19] C. Guo, W. Liao, Z. Li, C. Chen, Exploration of the catalytically active site structures of animal biomass-modified on cheap carbon nanospheres for oxygen reduction reaction with high activity, stability and methanol-tolerant performance in alkaline medium, Carbon 85 (2015) 279–288.

[20] Q. Wang, Q. Cao, X. Wang, B. Jing, H. Kuang, L. Zhou, A high-capacity carbon prepared from renewable chicken feather biopolymer for supercapacitors, J. Power Sources 225 (2013) 101—107.

[21] Y. Zheng, Z. Li, J. Xu, T. Wang, X. Liu, X. Duan, Y. Ma, Y. Zhou, C. Pei, Multi-channeled hierarchical porous carbon incorporated Co3O4 nanopillar arrays as 3D binder-free electrode for high performance supercapacitors, Nano Energy 20 (2016) 94—107.

[22] C. Long, D. Qi, T. Wei, J. Yan, L. Jiang, Z. Fan, Nitrogen-doped carbon networks for high energy density supercapacitors derived from polyaniline coated bacterial cellulose, Adv. Funct. Mater. 24 (2014) 3953—3961.

[23] H. Zhu, X. Wang, F. Yang, X. Yang, Promising carbons for supercapacitors derived from fungi, Adv. Mater. 23 (2011) 2745—2748.

[24] N. Guo, M. Li, Y. Wang, X. Sun, F. Wang, R. Yang, Soybean root-derived hierarchical porous carbon as electrode material for high-performance supercapacitors in ionic liquids, ACS Appl. Mater. Interfaces 8 (2016) 33626—33634.

[25] X. Wei, Y. Li, S. Gao, Biomass-derived interconnected carbon nanoring electrochemical capacitors with high performance in both strongly acidic and alkaline electrolytes, J. Mater. Chem. A 5 (2017) 181—188.

[26] J. Chang, Z. Gao, X. Wang, D. Wu, F. Xu, X. Wang, Y. Guo, K. Jiang, Activated porous carbon prepared from paulownia flower for high performance supercapacitor electrodes, Electrochim. Acta 157 (2015) 290—298.

[27] Y. Lv, L. Gan, M. Liu, W. Xiong, Z. Xu, D. Zhu, D.S. Wright, A self-template synthesis of hierarchical porous carbon foams based on banana peel for supercapacitor electrodes, J. Power Sources 209 (2012) 152—157.

[28] X.F. Tan, S.B. Liu, Y.G. Liu, Y.L. Gu, G.M. Zeng, X.J. Hu, X. Wang, S.H. Liu, L.H. Jiang, Biochar as potential sustainable precursors for activated carbon production: multiple applications in environmental protection and energy storage, Bioresour. Technol. 227 (2017) 359—372.

[29] N. Yoshizawa, K. Maruyama, Y. Yamada, M. Zielinska-Blajet, XRD evaluation of CO2 activation process of coal- and coconut shell-based carbons, Fuel 79 (2000) 1461—1466.

[30] J. Górka, M. Jaroniec, Hierarchically porous phenolic resin-based carbons obtained by block copolymer-colloidal silica templating and post-synthesis activation with carbon dioxide and water vapor, Carbon 49 (2011) 154—160.

[31] J. Wang, S. Kaskel, KOH activation of carbon-based materials for energy storage, J. Mater. Chem. 22 (2012) 23710—23725.

[32] X. Deng, B. Zhao, L. Zhu, Z. Shao, Molten salt synthesis of nitrogen-doped carbon with hierarchical pore structures for use as high-performance electrodes in supercapacitors, Carbon 93 (2015) 48—58.

[33] I.I.G. Inal, S.M. Holmes, A. Banford, Z. Aktas, The performance of supercapacitor electrodes developed from chemically activated carbon produced from waste tea, Appl. Surf. Sci. 357 (2015) 696—703.

[34] H. Lu, X.S. Zhao, Biomass-derived carbon electrode materials for supercapacitors, Sustain. Energy Fuels 1 (2017) 1265—1281.

[35] B. Liu, H. Chen, Y. Gao, H. Li, Preparation and capacitive performance of porous carbon materials derived from eulaliopsis binata, Electrochim. Acta 189 (2016) 93—100.

[36] T. Horibe, K. Yamada, Petal growth physiology of cut rose flowers: progress and future prospects, J. Hortic. Res. 25 (2017) 5—18.

[37] S.-w. Ryu, S. Choo, H.-J. Choi, C.-H. Kim, H. Lee, Replication of rose petal surfaces using a nickel electroforming process and UV nanoimprint lithography, Appl. Surf. Sci. 322 (2014) 57—63.

[38] Z. Xiao, X. Gao, M. Shi, G. Ren, G. Xiao, Y. Zhu, L. Jiang, China rose-derived tri-heteroatom co-doped porous carbon as an efficient electrocatalysts for oxygen reduction reaction, RSC Adv. 6 (2016) 86401—86409.

[39] B. Liu, Y. Liu, H. Chen, M. Yang, H. Li, Oxygen and nitrogen co-doped porous carbon nanosheets derived from Perilla frutescens for high volumetric performance supercapacitors, J. Power Sources 341 (2017) 309—317.

[40] C. Long, X. Chen, L. Jiang, L. Zhi, Z. Fan, Porous layer-stacking carbon derived from in-built template in biomass for high volumetric performance supercapacitors, Nano Energy 12 (2015) 141—151.

[41] J.C. Groen, L.A.A. Peffer, J. Pérez-Ramırez, Pore size determination in modified micro- and mesoporous materials. Pitfalls and limitations in gas adsorption data analysis, Microporous Mesoporous Mater. 60 (2003) 1—17.

[42] Z. Fan, Y. Liu, J. Yan, G. Ning, Q. Wang, T. Wei, L. Zhi, F. Wei, Template-directed synthesis of pillared-porous carbon nanosheet architectures: high-performance electrode materials for supercapacitors, Adv. Energy Mater. 2 (2012) 419—424.

[43] J. Qu, C. Geng, S. Lv, G. Shao, S. Ma, M. Wu, Nitrogen, oxygen and phosphorus decorated porous carbons derived from shrimp shells for supercapacitors, Electrochim. Acta 176 (2015) 982—988.

[44] M. Lee, G.P. Kim, H. Don Song, S. Park, J. Yi, Preparation of energy storage material derived from a used cigarette filter for a supercapacitor electrode, Nanotechnology 25 (2014), 345601.

[45] A. Ganesan, R. Mukherjee, J. Raj, M.M. Shaijumon, Nanoporous rice husk derived carbon for gas storage and high performance electrochemical energy storage, J. Porous Mater. 21 (2014) 839—847.

[46] M. Sevilla, W. Gu, C. Falco, M.M. Titirici, A.B. Fuertes, G. Yushin, Hydrothermal synthesis of microalgae-derived microporous carbons for electrochemical capacitors, J. Power Sources 267 (2014) 26—32.

[47] V. Subramanian, C. Luo, A.M. Stephan, K.S. Nahm, S. Thomas, B. Wei, Supercapacitors from activated carbon derived from banana fibers, J. Phys. Chem. C 111 (2007) 7527—7531.

[48] P. Yadav, A. Banerjee, S. Unni, J. Jog, S. Kurungot, S. Ogale, A 3D hexaporous carbon assembled from single-layer graphene as high performance supercapacitor, ChemSusChem 5 (2012) 2159—2164.

[49] G. Wang, X. Sun, F. Lu, H. Sun, M. Yu, W. Jiang, C. Liu, J. Lian, Flexible pillared graphene-paper electrodes for high-performance electrochemical supercapacitors, Small 8 (2012) 452—459.

[50] L. Deng, R.J. Young, I.A. Kinloch, A.M. Abdelkader, S.M. Holmes, D.A. De Haro-Del Rio, S.J. Eichhorn, Supercapacitance from cellulose and carbon nanotube nanocomposite fibers, ACS Appl. Mater. Interfaces 5 (2013) 9983—9990.

[51] X. Yu, Y. Wang, L. Li, H. Li, Y. Shang, Soft and wrinkled carbon membranes derived from petals for flexible supercapacitors, Sci. Rep. 7 (2017) 45378.

[52] T. Ouyang, K. Cheng, Y. Gao, S. Kong, K. Ye, G. Wang, D. Cao, Molten salt synthesis of nitrogen doped porous carbon: a new preparation methodology for high-volumetric capacitance electrode materials, J. Mater. Chem. A 4 (2016) 9832—9843.

[53] E. Frackowiak, Q. Abbas, F. Béguin, Carbon/carbon supercapacitors, J. Energy Chem. 22 (2013) 226—240.

[54] P. Sun, H. Yi, T. Peng, Y. Jing, R. Wang, H. Wang, X. Wang, Ultrathin MnO2 nanoflakes deposited on carbon nanotube networks for symmetrical supercapacitors with enhanced performance, J. Power Sources 341 (2017) 27—35.

[55] L. Zhao, J. Yu, W. Li, S. Wang, C. Dai, J. Wu, X. Bai, C. Zhi, Honeycomb porous MnO2 nanofibers assembled from radially grown nanosheets for aqueous supercapacitors with high working voltage and energy density, Nano Energy 4 (2014) 39—48.

[56] B. Liu, X. Zhou, H. Chen, Y. Liu, H. Li, Promising porous carbons derived from lotus seedpods with outstanding supercapacitance performance, Electrochim. Acta 208 (2016) 55—63.

[57] H. Feng, H. Hu, H. Dong, Y. Xiao, Y. Cai, B. Lei, Y. Liu, M. Zheng, Hierarchical structured carbon derived from bagasse wastes: a simple and efficient synthesis route and its improved electrochemical properties for high-performance supercapacitors, J. Power Sources 302 (2016) 164—173.

[58] D. Zeng, Y. Dou, M. Li, M. Zhou, H. Li, K. Jiang, F. Yang, J. Peng, Wool fiber-derived nitrogen-doped porous carbon prepared from molten salt carbonization method for supercapacitor application, J. Mater. Sci. 53 (2018) 8372—8384.

[59] G. Ma, J. Li, K. Sun, H. Peng, E. Feng, Z. Lei, Tea-leaves based nitrogen-doped porous carbons for high-performance supercapacitors electrode, J. Solid State Electrochem. 21 (2017) 525—535.

[60] H. Peng, G. Ma, K. Sun, Z. Zhang, Q. Yang, Z. Lei, Nitrogen-doped interconnected carbon nanosheets from pomelo mesocarps for high performance supercapacitors, Electrochim. Acta 190 (2016) 862—871.

[61] M. Rana, K. Subramani, M. Sathish, U.K. Gautam, Soya derived heteroatom doped carbon as a promising platform for oxygen reduction, supercapacitor and CO2 capture, Carbon 114 (2017) 679—689.

[62] L. Xin, R. Li, Z. Lu, Q. Liu, R. Chen, J. Li, J. Liu, J. Wang, Hierarchical metal-organic framework derived nitrogen-doped porous carbon by controllable synthesis for high performance supercapacitors, J. Electroanal. Chem. 813 (2018) 200—207.

[63] J. Yang, J. Hu, M. Zhu, Y. Zhao, H. Chen, F. Pan, Ultrahigh surface area meso/microporous carbon formed with self-template for high-voltage aqueous supercapacitors, J. Power Sources 365 (2017) 362—371.

[64] S. Lei, L. Chen, W. Zhou, P. Deng, Y. Liu, L. Fei, W. Lu, Y. Xiao, B. Cheng, Tetraheteroatom self-doped carbon nanosheets derived from silkworm excrement for high-performance supercapacitors, J. Power Sources 379 (2018) 74—83.

[65] Y.-K. Hsu, Y.-C. Chen, Y.-G. Lin, L.-C. Chen, K.-H. Chen, High-cell-voltage supercapacitor of carbon nanotube/carbon cloth operating in neutral aqueous solution, J. Mater. Chem. 22 (2012) 3383—3387.

[66] Y. Zhang, Z. Hu, Y. An, B. Guo, N. An, Y. Liang, H. Wu, High-performance symmetric supercapacitor based on manganese oxyhydroxide nanosheets on carbon cloth as binder-free electrodes, J. Power Sources 311 (2016) 121—129.

[67] M. Inagaki, H. Konno, O. Tanaike, Carbon materials for electrochemical capacitors, J. Power Sources 195 (2010) 7880—7903.

[68] P. Cheng, S. Gao, P. Zang, X. Yang, Y. Bai, H. Xu, Z. Liu, Z. Lei, Hierarchically porous carbon by activation of shiitake mushroom for capacitive energy storage, Carbon 93 (2015) 315—324.

[69] L. Sun, C. Tian, M. Li, X. Meng, L. Wang, R. Wang, J. Yin, H. Fu, From coconut shell to porous graphene-like nanosheets for high-power supercapacitors, J. Mater. Chem. A 1 (2013) 6462—6470.

[70] F. Ma, J. Wan, G. Wu, H. Zhao, Highly porous carbon microflakes derived from catkins for high-performance supercapacitors, RSC Adv. 5 (2015) 44416—44422.